Physica D 240 (2011) 1701–1713

Contents lists available at SciVerse ScienceDirect

Physica D

journal homepage: www.elsevier.com/locate/physd

Maximizing critical currents in superconductors by optimization of normal inclusion properties

Yanzhi Zhang [a,*], Janet Peterson [b], Max Gunzburger [b]

[a] Department of Mathematics and Statistics, Missouri University of Science and Technology, Rolla, MO 65409-0020, United States

[b] Department of Scientific Computing, Florida State University, Tallahassee, FL 32306-4120, United States

ARTICLE INFO

Article history:
Received 21 December 2010
Received in revised form
13 May 2011
Accepted 27 June 2011
Available online 28 July 2011
Communicated by Thomas Wanner

Keywords:
Superconductivity
Critical currents
Vortex pinning
Ginzburg–Landau equations
Optimal control

ABSTRACT

The movement of vortices in superconductors due to an applied current can induce a loss of perfect conductivity. Experimental observations show that material impurities can effectively prevent vortices from moving. In this paper, we provide numerical studies to investigate vortex pinning and critical currents through the use of an optimal control approach applied to a variant of the time-dependent Ginzburg–Landau model that can account for normal inclusions. The effects that the size and boundary of the sample and the number, size, shape, orientation, and location of the inclusion sites have on the critical current and vortex lattices are studied. In particular, the optimal control approach is used to determine the optimal properties of the impurities so as to maximize the critical current, i.e., the largest current that can pass through a superconductor without resistance.

1. Introduction

Since its discovery in 1910, superconductivity has attracted the intense interest of researchers. More recently, the discovery of high-temperature superconductors (HTS) has further stimulated interest in this field. The great interest in superconductors is due to their fascinating property of zero resistivity or infinite conductivity; that is, below a critical temperature and below a critical external magnetic field, superconducting materials can conduct electric currents without resistance. However, a critical factor limiting the practical application of superconductors is their response to magnetic fields that can create tubes of magnetic flux referred to as superconducting vortices. In the presence of an applied current, these vortices start moving, and their movement can reduce or eliminate the amount of resistanceless current a superconducting material can carry. Thus, pinning vortices in a superconductor and increasing its critical current are important issues in superconductivity research. Here, we define the critical current as the largest applied current that can pass through a superconductor while all the vortices remain stationary.

Experimentally, vortex pinning has been realized using several mechanisms such as adding defects or impurities in superconductors [1–3], varying the thickness of the thin films [4], and using grain and twin boundaries in anisotropic superconductors [5]. Among these mechanisms, doping impurities (i.e., normal inclusions) may be the most popular because impurities can be easily manipulated in several ways to increase the critical current. Impurities act as pinning centres that can result in an increase in the critical current at higher magnetic fields. In addition, the material composition of impurities as well as their number, shape, and location can have an important influence on superconducting properties [1–3].

Computationally, the properties of superconducting vortices have been extensively studied by using the well-known Ginzburg–Landau (GL) model for superconductivity [6–8]. For example, vortex structure and vortex pinning are investigated by using the normal inclusion GL models in [9–12]. Similar studies were also carried out in [13,11] by using the variable thickness thin-film GL models. In [14,15], the influence of random thermal fluctuations on vortex structure was also studied by simulating stochastic GL models. The interaction and dynamics of vortices were investigated in [16–18]. On the other hand, the properties of superconductors have been investigated through different optimal control approaches subject to the GL models. For example, to meet a desired superconducting state, an optimal control problem using a boundary control was considered in [19]. In [20–22], the external magnetic field was controlled by using the variable thickness thin-film GL model. Recently, critical current enhancement was studied in [23] by controlling the placement of normal inclusions.

* Corresponding author. Tel.: +1 573 341 4651; fax: +1 573 341 4741.
E-mail addresses: zhangyanz@mst.edu (Y. Zhang), jpeterson@fsu.edu (J. Peterson), gunzburg@fsu.edu (M. Gunzburger).

0167-2789/$ – see front matter © 2011 Elsevier B.V. All rights reserved.
doi:10.1016/j.physd.2011.06.024

In this paper, we study the pinning of vortices by embedding normal inclusions into a superconducting material and then determining the critical current through an optimal control approach. By introducing a cost functional, we cast the problem into an optimization problem, that is, we minimize the cost functional with respect to some control parameters. A similar cost functional was used in [23] with the optimization parameters chosen as the centres of inclusion sites and the applied current. We employ additional optimization parameters. To gain insight, we first choose the applied current as the only control parameter and numerically study the effect of the sample boundary and the properties of the inclusion sites, e.g., their number, size, shape, orientation, and location, on the pinning of vortices and the critical current. Then, we add the size and location of each inclusion site as additional control parameters and report and compare the optimal results for some representative cases.

The paper is organized as follows. In Section 2, we briefly review a variant of the time-dependent Ginzburg–Landau model for superconductivity that can account for normal inclusions. Then, an optimal control approach and its numerical realization are discussed in Section 3. In Section 4, vortex pinning and the critical current are studied by solving an optimization problem with different control parameters. Finally, some concluding remarks are made in Section 5.

2. Ginzburg–Landau model

The two-dimensional, time-dependent Ginzburg–Landau (TDGL) model used in our study is well-known for describing the properties of superconductors. Details may be found in [9,6,8]. A variant of that model that can account for normal inclusions was given in [9]. We let $\Omega = [0, L]^2$ denote the domain occupied by the sample and $\Gamma = \partial\Omega$ its boundary. Assume that a constant external magnetic field $\mathbf{H}$ is applied in the direction perpendicular to the sample surface, i.e., $\mathbf{H} = H\widehat{\mathbf{z}}$, where $\widehat{\mathbf{z}}$ denotes the unit vector in the z-direction and $H = |\mathbf{H}|$ denotes the magnitude of $\mathbf{H}$. In addition, we assume that an applied current $\mathbf{J}$ is injected in the y-direction, i.e., $\mathbf{J} = J\widehat{\mathbf{y}}$, with J a constant in time, where $\widehat{\mathbf{y}}$ denotes the unit vector in the y direction.

After a suitable nondimensionalization, the dimensionless TDGL equations for the complex scalar-valued order parameter ψ and real vector-valued magnetic potential $\mathbf{A}$ are given by [9,6,23]

$$\frac{\partial\psi}{\partial t} + \left(i\xi\nabla + \frac{1}{\kappa}\mathbf{A}\right)^2\psi + (|\psi|^2+\alpha)\psi - i\frac{Jy}{\nu\kappa}\psi = 0 \quad \text{in } \Omega, \tag{2.1}$$

$$\frac{\nu}{\xi^2}\frac{\partial\mathbf{A}}{\partial t} + \nabla\times\nabla\times\mathbf{A} + \frac{i}{2\kappa}(\psi^*\nabla\psi - \psi\nabla\psi^*) + \frac{1}{\lambda^2}|\psi|^2\mathbf{A} - \mathbf{J} = \nabla\times\mathbf{H} \quad \text{in } \Omega, \tag{2.2}$$

where $(\cdot)^*$ denotes the complex conjugate, along with the boundary conditions

$$\left(i\xi\nabla\psi + \frac{1}{\kappa}\mathbf{A}\psi\right)\cdot\mathbf{n} = 0 \quad \text{on } \Gamma, \tag{2.3}$$

$$\nabla\times\mathbf{A}\times\mathbf{n} = \left(\mathbf{H} - \left(x - \frac{L}{2}\right)J\widehat{\mathbf{z}}\right)\times\mathbf{n} \quad \text{on } \Gamma, \tag{2.4}$$

$$\mathbf{A}\cdot\mathbf{n} = 0 \quad \text{on } \Gamma, \tag{2.5}$$

with $\mathbf{n}$ denoting the unit normal vector on Γ. In (2.1)–(2.5), the coherence length ξ describes the size of thermodynamic fluctuations in the superconducting phase, and the London penetration length λ describes the distance over which the magnetic field can penetrate into the superconductor. The ratio $\kappa = \lambda/\xi$ denotes the Ginzburg–Landau parameter, and $\nu > 0$ is a relaxation parameter. The parameter α is temperature-dependent and is discussed later. The order parameter ψ can be viewed as the wave function of the superconducting electrons, with its magnitude $|\psi|$ proportional to the density of such electrons. In the above nondimensionalized form, $|\psi| = 1$ means that the material is in a pure superconducting state, while $|\psi| = 0$ represents the normal state.

The initial conditions of the TDGL equations (2.1)–(2.5) are given by

$$\psi(\mathbf{x}, 0) = \psi_0(\mathbf{x}) \quad \text{and} \quad \mathbf{A}(\mathbf{x}, 0) = \mathbf{A}_0(\mathbf{x}) \quad \text{in } \Omega, \tag{2.6}$$

where we assume that $\nabla\cdot\mathbf{A}_0 = 0$ and also that $|\psi_0(\mathbf{x})| \le 1$, *a.e.*. It is well known that the Ginzburg–Landau equations are gauge invariant. To ensure that the solutions are unique, we have applied the following gauges in (2.1)–(2.6):

$$-\nabla\Phi = \mathbf{J} \quad \text{in } \Omega \quad \text{and} \quad \mathbf{A}\cdot\mathbf{n} = 0 \quad \text{on } \Gamma, \tag{2.7}$$

i.e., choosing a nonzero electric potential Φ and setting the normal component of the magnetic potential to be zero on the boundary Γ. Eq. (2.7) immediately implies that the electric potential $\Phi = -Jy$. It is known that solutions of the TDGL equations (2.1)–(2.6) are unique up to the gauge transformation (2.7); see more details in [6,24,25].

As mentioned above, the parameter α in (2.1) is temperature-dependent, and thus the term $\alpha\psi$ describes the material properties at a given temperature. Below the critical temperature of a superconductor, the parameter $\alpha < 0$ in the regions occupied by superconducting materials, while $\alpha > 0$ in those with normal materials. In particular, after nondimensionalization, $\alpha \equiv -1$ for a pure superconducting state. Thus, the TDGL equations (2.1)–(2.6) provide an effective model for describing a superconducting sample embedded with impurities (i.e., normal inclusions), and the properties of the normal inclusions can be easily controlled by adjusting the parameter α in (2.1) [9].

For an integer M, we assume that M normal inclusions are embedded in the superconducting sample and each has the same shape. Let $D_m := D(\mathbf{x}_m)$ (for $m = 1, \ldots, M$) denote the region occupied by the m-th inclusion, with $\mathbf{x}_m$ representing its mass centre. Assume that the impurities have uniform material properties and thus the point $\mathbf{x}_m$ is also the geometric centre of the m-th inclusion. In the following, we define

$$\alpha := \alpha(\mathbf{x}) = \begin{cases} 1 & \text{if } \mathbf{x}\in D_m, \text{ for } m = 1,\ldots,M \\ -1 & \text{otherwise} \end{cases} \tag{2.8}$$

in (2.1), that is, we set $\alpha = 1$ for the normal inclusion regions and $\alpha = -1$ for the superconducting regions.

3. Optimal control approach

Recently, an optimal control problem was proposed in [23] to determine the locations of normal inclusion sites that result in the largest critical current. In that work, a fixed number of circular normal inclusion regions of the same size were used and a cost functional involving their centres and the applied current was introduced. If we use additional parameters as control parameters, then the cost functional has the general form

$$\mathcal{F}(\psi, P, J) = \int_{T_1}^{T_2}\int_\Omega\left(\frac{\partial|\psi|}{\partial t}\right)^2 \mathrm{d}\mathbf{x}\,\mathrm{d}t - \mu J^2, \tag{3.1}$$

where P denotes the set of parameters used and which are discussed later. The first term in (3.1) is used to measure the motion of the vortices in the time interval $[T_1, T_2]$, which depends on the properties of the normal inclusions through the parameter $\alpha(\mathbf{x})$ given in (2.8) and used in (2.1). For a given configuration of inclusion sites, if the applied current J is smaller than the critical current, then a stationary state is reached after a sufficiently large time T_1. In this case, all vortices remain motionless for any time $t \geq T_1$, and the first term in (3.1) is zero. The second term in (3.1) is a penalty term. The positive constant μ is used to adjust the relative importance of the two terms and is chosen to meet the requirements that if the applied current is smaller than the critical current, i.e., $J < J_c$, the second term in (3.1) is dominant, while the first term becomes significant when $J > J_c$.

The parameter P in (3.1) is used to denote a set of parameters characterizing the normal inclusions which play an important role in vortex pinning. For example, P represented the locations of the M normal inclusion sites in [23] as determined by their geometric centres, i.e., $P = \{\mathbf{x}_m\}_{m=1}^{M}$. In fact, other properties, e.g., the size and shape, of the normal inclusions also influence the pinning of vortices. Without loss of generality, we denote

$$P = \{P_m\}_{m=1}^{M} \quad \text{with } P_m = \{p_{m,k}\}_{k=1}^{q}, \tag{3.2}$$

where we assume that there are q parameters for each of the inclusion sites, and P_m is the parameter set for the m-th site. For example, when only the centre of each inclusion site is used, $P_m = \{x_m, y_m\}$ and $q = 2$.

After introducing the cost functional $\mathcal{F}(\psi, P, J)$, we translate the problem of seeking the critical current and the inclusion site parameters into an optimal control problem. Specifically, we seek the state variables $(\psi, \mathbf{A})$ and the control variables (P, J) such that the functional $\mathcal{F}$ defined in (3.1) is minimized subject to the requirements that $(\psi, \mathbf{A})$ and (P, J) satisfy the TDGL equations (2.1)–(2.6), i.e.,

$$\min_{(P,J)} \mathcal{F}(\psi, P, J) \quad \text{subject to (2.1)–(2.6)}. \tag{3.3}$$

Then, the optimization problem (3.3) can be solved by using standard techniques; in this work, we use the gradient method, where the gradients of the functional $\mathcal{F}$ with respect to the control variables are determined through sensitivity derivatives [26]. After we determine $-\nabla\mathcal{F}$, we take a step along this direction, using the appropriate step lengths for each parameter that ensures that the cost functional decreases.

For convenience, we denote $S = \{s_l\}_{l=1}^{qM+1}$ as the set of all control variables. Let

$$\psi_l' = \frac{\partial \psi}{\partial s_l} \quad \text{and} \quad \mathbf{A}_l' = \frac{\partial \mathbf{A}}{\partial s_l} \quad \text{for } l = 1, \ldots, qM+1 \tag{3.4}$$

denote the sensitivity derivative of the state variables $(\psi, \mathbf{A})$ with respect to the l-th control variable. By directly differentiating the state equations (2.1)–(2.6) with respect to the control variable s_l, we get the following sensitivity equations for each s_l, $l = 1, \ldots, qM+1$:

$$\begin{aligned}
&\frac{\partial \psi_l'}{\partial t} + \left(i\xi\nabla + \frac{1}{\kappa}\mathbf{A}\right)^2 \psi_l' + \frac{2}{\kappa}\left(i\xi\nabla + \frac{1}{\kappa}\mathbf{A}\right)\cdot \mathbf{A}_l'\psi + \psi^2(\psi_l')^* \\
&\quad + \left(2|\psi|^2 + \alpha(\mathbf{x}) - i\frac{Jy}{\nu\kappa}\right)\psi_l' \\
&= \left(-\frac{\partial \alpha(\mathbf{x})}{\partial s_l} + i\frac{y}{\nu\kappa}\frac{\partial J}{\partial s_l}\right)\psi \quad \text{in } \Omega,
\end{aligned} \tag{3.5}$$

$$\begin{aligned}
&\frac{\nu}{\xi^2}\frac{\partial \mathbf{A}_l'}{\partial t} + \nabla\times\nabla\times\mathbf{A}_l' \\
&\quad + \frac{i}{2\kappa}\left((\psi_l^*)'\nabla\psi + \psi^*\nabla\psi_l' - \psi_l'\nabla\psi^* - \psi\nabla(\psi_l')^*\right) \\
&\quad + \frac{1}{\lambda^2}\left[|\psi|^2\mathbf{A}_l' + \left(\psi_l'\psi^* + \psi(\psi_l')^*\right)\mathbf{A}\right] = \frac{\partial(\nabla\times\mathbf{H})}{\partial s_l} + \frac{\partial \mathbf{J}}{\partial s_l} \\
&\text{in } \Omega,
\end{aligned} \tag{3.6}$$

together with the boundary conditions

$$\left[\left(i\xi\nabla + \frac{1}{\kappa}\mathbf{A}\right)\psi_l' + \frac{1}{\kappa}\mathbf{A}_l'\psi\right]\cdot\mathbf{n} = 0 \quad \text{on } \Gamma, \tag{3.7}$$

$$\nabla\times\mathbf{A}_l'\times\mathbf{n} = \left[\frac{\partial \mathbf{H}}{\partial s_l} - \left(x - \frac{L}{2}\right)\frac{\partial J}{\partial s_l}\widehat{\mathbf{z}}\right]\times\mathbf{n} \quad \text{on } \Gamma, \tag{3.8}$$

$$\mathbf{A}_l'\cdot\mathbf{n} = 0 \quad \text{on } \Gamma, \tag{3.9}$$

and the initial conditions

$$\psi_l'(\mathbf{x}, 0) = 0 \quad \text{and} \quad \mathbf{A}_l'(\mathbf{x}, 0) = \mathbf{0} \quad \text{in } \Omega. \tag{3.10}$$

Then, the sensitivities ψ_l' and $\mathbf{A}_l'$ (for $l = 1, \ldots, qM+1$) can be obtained by solving the sensitivity system (3.5)–(3.10).

Numerically, we choose to discretize the TDGL equations (2.1)–(2.6) by a finite element method in space and by a backward differentiation multi-step method in time, and to solve the resulting nonlinear system by Newton's method. The global existence and uniqueness of the solutions of (2.1)–(2.6) have been proved in a limit sense, and the corresponding error estimates have been studied in [24,25,23]. The sensitivity equations (3.5)–(3.10) are discretized in the same manner. However, the discretization of (3.5)–(3.10) results in a linear system for each control variable s_l. Furthermore, for each s_l, the resulting linear system has the same coefficient matrix, and only the right-hand side vectors differ. Thus, in the computations, we need to assemble the coefficient matrix only once and apply it to solve for all the control variables. See [23] for details of the algorithm in the case where $P_m = \{x_m, y_m\}$ and $q = 2$ in (3.2).

4. Numerical results

In this section, we numerically study vortex pinning and critical currents for different inclusion configurations. For all computations except those in Section 4.1.4, the normal inclusion sites are chosen to be circular and defined by

$$D_m = \{\mathbf{x} : |\mathbf{x} - \mathbf{x}_m| < r_m\} \quad \text{for } 1 \leq m \leq M \tag{4.1}$$

with $\mathbf{x}_m$ and r_m the centre and radius of the m-th inclusion site, respectively. In Section 4.1.4, we consider alternative shapes of the impurities.

The control algorithm is computationally intensive. Although the sensitivity equations are linear and share the same coefficient matrix, it must be assembled at each time step; furthermore, the more control parameters one uses, the more steps of the gradient method are typically required. For computational reasons, we have broken our simulations into two parts. In the first part, we have chosen only J as the control parameter to reduce the computational cost. Hence, we study the effects on the critical current of the sample boundary and the number, size, shape, orientation, and location of the normal inclusion sites, all of which are fixed during the optimization procedure. This will give us insight into the parameters which are the most important. In the second part of our simulations, we include various parameters for each inclusion site as control variables in addition to the current so as to determine, e.g., the optimal location, shape, etc. of those inclusions.

For all simulations, the parameters in the TDGL equations (2.1)–(2.6) and the sensitivity equations (3.5)–(3.10) are chosen as follows: $\xi = 0.1$, $\kappa = 5.0$, $\nu = 1$ and $\lambda = \xi\kappa = 0.5$. In addition, a constant magnetic field with magnitude $H = \kappa/2 = 2.5$ is applied in the z-direction; this nondimensional magnetic field corresponds to one-half the bulk upper critical field H_{c_2}. At each control step, we choose the initial condition as the steady state corresponding to the current configuration of inclusion sites and the applied current $J = 0$, that is, the applied current is turned on at time $t = 0$. The sample domain is chosen to be a square with side $L = a\xi$

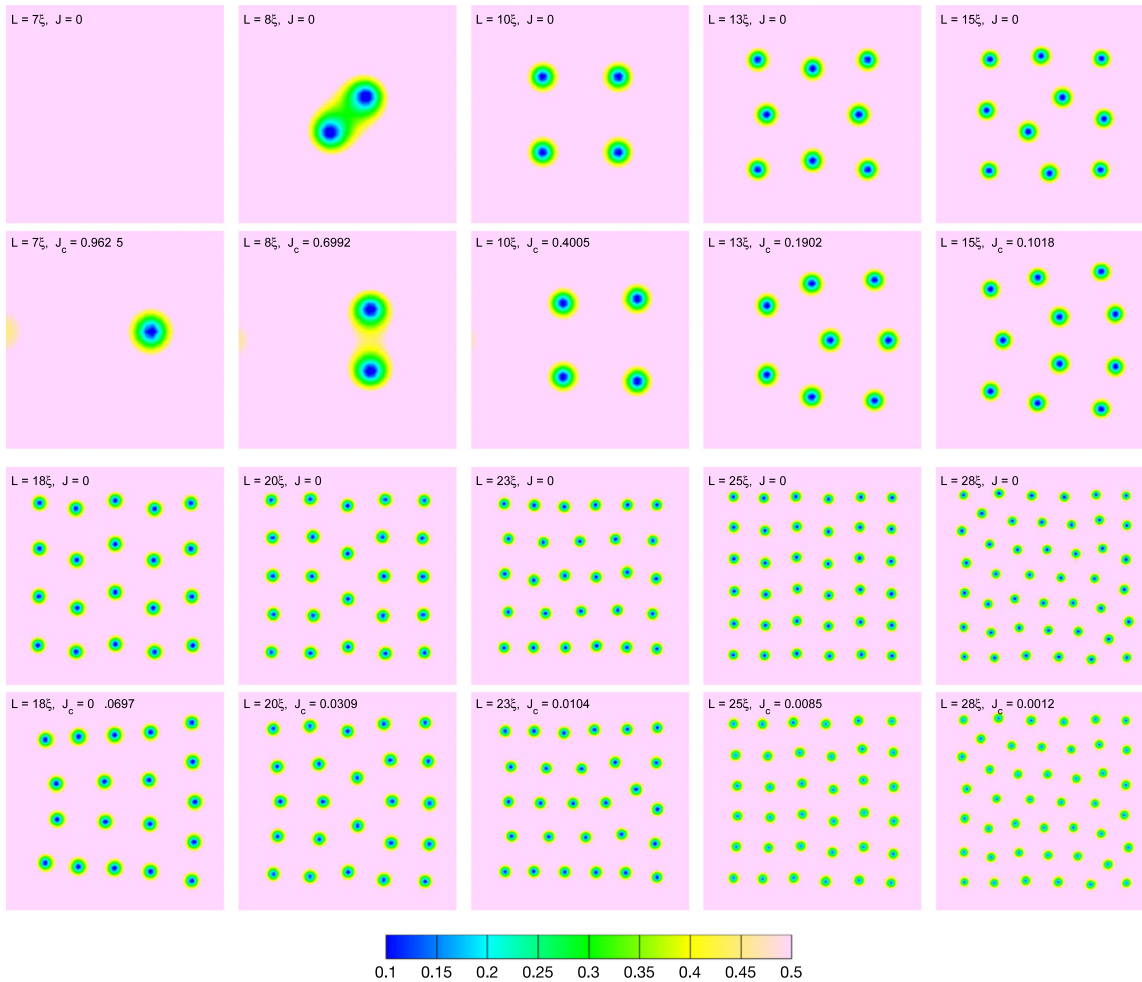

Fig. 1. Stationary vortex lattices for $J = 0$ (first and third rows) and for the critical current J_c (second and fourth rows) for different sample sizes $L = a\xi$, a and integer, with no normal inclusions.

($a > 0$). Numerically, the finite element spaces are constructed by using continuous piecewise quadratic polynomials [24,11,7,23]. The time step is chosen to ensure that the computation is efficient and, on the other hand, the accumulated errors from time discretization are insignificant after a long time. We have found that a time step $\Delta t = 0.2$ is satisfactory in this regard. In the cost functional (3.1), the motion of the superconducting vortices is measured in a time period with length 500, i.e., $T_2 = T_1 + 500$. To get an effective control, we have to choose different μ and T_1 depending on the sample size L. In particular, the time T_1 should be large enough to ensure that in the case of $J < J_c$, the steady state is already reached at the time $t = T_1$. For example, we use $\mu = 10^{-4}$ and $T_1 = 5600$ when the sample size $L = 20\xi$, whereas when $L = 10\xi$, we take $\mu = 10^{-8}$ and $T_1 = 2200$.

For plotting purposes, we rewrite the order parameter in the form

$$\psi(\mathbf{x}, t) = \sqrt{\rho(\mathbf{x}, t)}\exp(iS(\mathbf{x}, t)), \tag{4.2}$$

where $\rho(\mathbf{x}, t) = |\psi|^2$ and $S(\mathbf{x}, t) = \arg(\psi)$ are the position density and phase of $\psi(\mathbf{x}, t)$, respectively. The numerical results are displayed in the form of density ρ, where the normal inclusion sites are indicated by the closed regions illustrated by black lines. For clarity, we only plot $|\psi| \leq 0.5$ in the density plots. To get a better view of the vortex distribution, the phase plots are also presented; here the symbol '+' represents the centre of a vortex with winding number $+1$. The winding number ω (also known as the topological charge) of a vortex is defined by

$$\omega = \frac{1}{2\pi}\oint_{\mathcal{C}} \nabla S \cdot d\mathbf{l}, \tag{4.3}$$

where $\mathcal{C}$ is a closed curve containing the vortex centre.

4.1. Studies with the single control parameter J

In this section, we consider vortex pinning in the simplified case where the applied current is the only control variable; all parameters that determine the configuration of the normal inclusions are held fixed during the optimization process. First, the pinning effect of the boundary is studied by considering different sample sizes with $L = a\xi$ for integer a. Then, in Sections 4.1.2, 4.1.3 and 4.1.5, we investigate the effects of the number, size, and locations of the circular inclusion sites, respectively, where we use the same radius for all inclusion sites, i.e., $r_m = r$ for $1 \leq m \leq M$. In addition, vortex pinning by square and elliptic inclusion sites are studied in Section 4.1.4.

4.1.1. Boundary effects

Computationally, we consider finite sample sizes, so that the boundary influences the nucleation of vortices [27]. Before adding normal inclusions as pinning sites, we consider the pinning effect of the boundary as the sample size increases. First, for each sample size, the state equations (2.1)–(2.6) are approximated with $\alpha(\mathbf{x}) \equiv -1$ and $J = 0$ until a steady state is reached. Next, to see how the critical current behaves as the sample size increases, we solve the optimal control problem (3.3) with J the only control parameter.

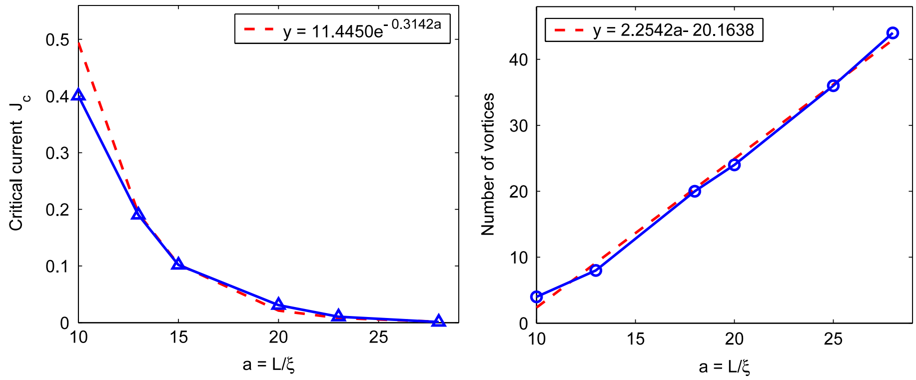

Fig. 2. For no normal inclusions, on the left, the critical current J_c versus the ratio $a = L/\xi$; the curve fit shown by the dashed curve is given by $y \approx 11.45e^{-0.3142a}$. On the right, the number of vortices versus a for $J = 0$; the linear fit shown by the dashed line is given by $y = 2.254a - 20.16$.

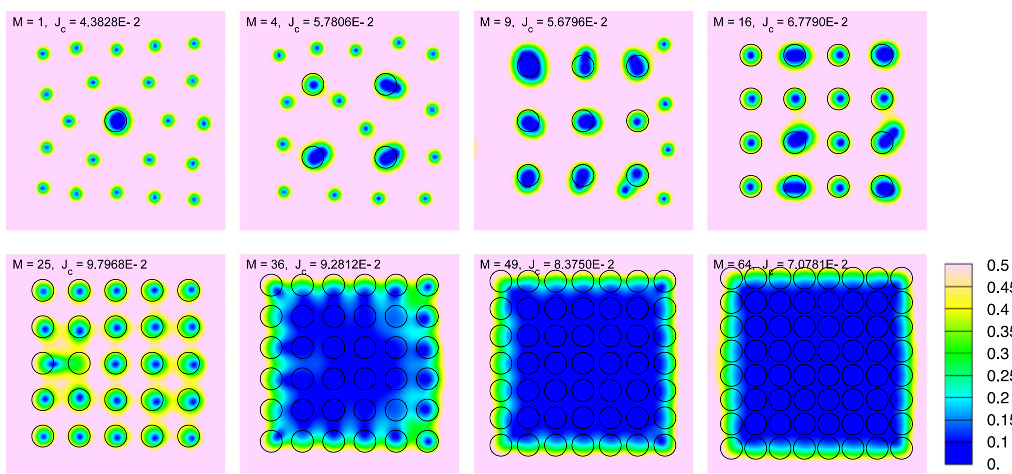

Fig. 3. Vortex pinning and critical current with M circular normal inclusion sites which have a radius $r = \xi$ for a sample of size $L = 20\xi$.

Fig. 1 displays the stationary vortex lattices for the sample size of $L = a\xi$ for 10 values of a between 7 and 28 for the solutions of the TDGL equations with $J = 0$ and for $J = J_c$, where the value of J_c is obtained through the optimal control algorithm. We note that when the current $J = 0$, if the size L is too small, e.g., $L \leq 7\xi$, no vortex is nucleated in the sample; a stationary vortex lattice is achieved for the larger values of L. Furthermore, the larger the sample, the more vortices in the lattice. The vortex lattices always have a certain symmetry when $J = 0$, but they are slightly twisted if a nonzero current $J < J_c$ is applied. Furthermore, due to the fact that the current is applied in the y-direction, all vortices are shifted to the right compared to their positions when $J = 0$. In addition, if the applied current $J > J_c$, the vortices move and, during the time evolution, they periodically come into the lattice from the left side of the sample and leave at the right side.

Fig. 1 also suggests that although no normal inclusions are applied, the sample still allows small nonzero applied currents, e.g., $0 < J \leq J_c$, to pass through, while the vortices remain stable, which agrees with the theoretical results in [28]. This confirms that the boundary of the sample has a pinning effect on vortices. However, the boundary pinning becomes weaker as the sample size increases, which can be also observed in Fig. 2 which shows the relations between the sample size L and both the critical current J_c and the number of vortices nucleated in the lattices when $J = 0$. The results show that the number of vortices present in the lattices increases roughly linearly with sample size. In contrast, the critical current exponentially decreases for increasing sample size L.

4.1.2. *Effect of number of inclusion sites*

We now consider the effect that the number of normal inclusion sites has on the critical current and the number of vortices. For these simulations, we assume that all inclusions are uniformly distributed inside a fixed sample of size $L = 20\xi$ and have circular shapes with the same radius $r = \xi$. Next, we attempt to quantify the number of inclusions which provides the highest critical current; this, of course, depends on the sample size. In all simulations, the critical current is determined by minimizing the cost functional defined in (3.1) with the parameters in the set P that determine the configuration of the inclusions held fixed during the optimization process.

Fig. 3 shows the vortex pinning and the critical current as the number of normal inclusion sites is increased from $M = 1$ to $M = 64$. Fig. 4 displays the phase plots for the cases $M = 1, 4, 25$, and 49. Comparing with Fig. 1 for $L = 20\xi$, we find that the structure of the vortex lattices is very different when normal inclusions are added to the sample; in addition, the number of vortices present in the sample is also influenced by the number of inclusions used. For example, in a clean sample the stationary lattice is composed of 24 vortices, while only 23 vortices appear when $M = 1$ or 9, and the number becomes 25 when $M = 49$; see Fig. 4. In addition, Fig. 4 shows that if the number of inclusion sites is smaller than that of vortices, each site can attract and pin more than one vortex. For example, when $M = 1$, the inclusion site pins two vortices, and the other 21 remain free from the pinning site. If the number of inclusions is large, then each vortex is strongly pinned by one or more inclusion sites.

From the results in Fig. 3, we observe that for the sample size $L = 20\xi$, the critical current ranges from approximately 0.0438 to 0.0980. Moreover, the maximum critical current does not occur when the number of inclusion sites is the largest. The critical current increases and then decreases as more inclusion sites are used. We want to ascertain the number of inclusion sites which

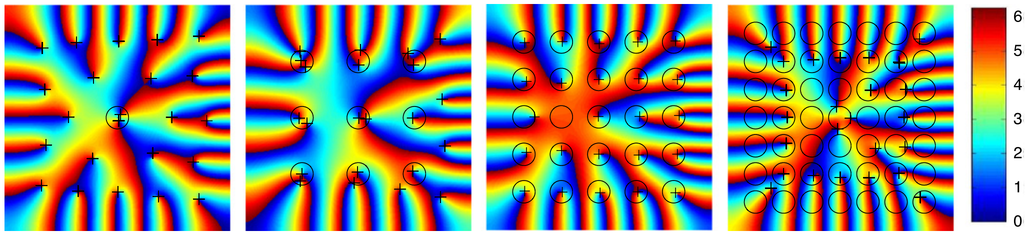

Fig. 4. Phase plots of stationary vortex lattices for different numbers of normal inclusion sites when the critical current J_c is applied, where the radius of the circular inclusions is $r = \xi$ and the sample size $L = 20\xi$.

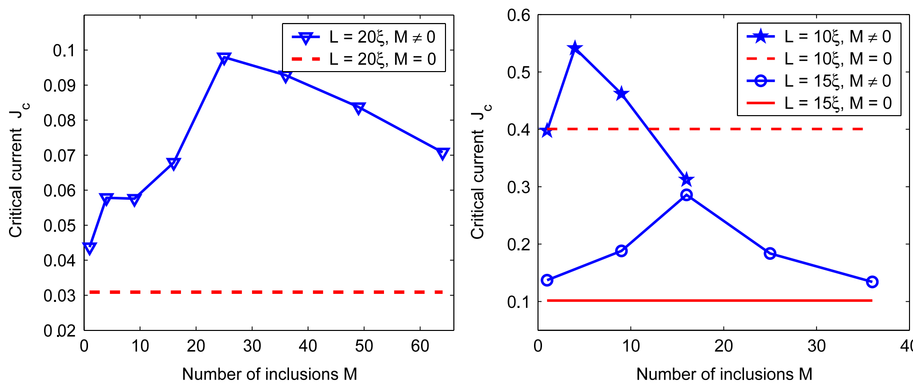

Fig. 5. Critical current J_c versus the number of normal inclusion sites for the sample size $L = 20\xi$ (left), and $L = 10\xi$ and 15ξ (right), where the inclusion radius $r = \xi$ is fixed. The horizontal lines give the critical currents for the case of no normal inclusions.

maximizes J_c for each sample size. In Fig. 5 we show the relation between the critical current and the number of inclusion sites for the samples of sizes $L = 10\xi$, 15ξ, and 20ξ.

We find that for a given sample size L, there exists a number $M_{L,c}$ such that for $M < M_{L,c}$, the more the inclusion sites, the larger the critical current, whereas the critical current J_c decreases as M increases when $M > M_{L,c}$. To understand why this is true, we note that when the number of inclusion sites is small, many vortices are unpinned and they can be easily moved by an applied current. Thus, to keep them stationary, only a small amount of current is allowed. In addition, in this case, two or three vortices may be pinned by the same inclusion site and, because vortices have a repulsive interaction on each other, it is easy for them to escape from the inclusion site when a current is applied. On the other hand, if M is large, then all vortices are strongly locked by the inclusion sites, which requires a larger current to move them, but if the number of inclusions is too large, then the superconducting material is highly "polluted", which also reduces the superconductivity and decreases the critical current. Fig. 5 also suggests that the number $M_{L,c}$ is around the number of vortices present in the sample when $J = 0$. For example, we have $M_{10\xi,c} \approx 4$, $M_{15\xi,c} \approx 10$, and $M_{20\xi,c} \approx 24$.

4.1.3. *Effect of size of inclusion sites*

Experimental observations show that not only the number but the size of the normal inclusion sites can influence the pinning of superconducting vortices. To better understand this phenomenon and to see the effects on the critical current, we fix the sample size to $L = 20\xi$ and set the number of circular normal inclusion sites to $M = 4$. We uniformly distribute the four identical inclusions inside the sample and then see the effect as the radius of the sites is increased.

In Fig. 6, we plot the stationary vortex lattices and give the critical current resulting from the control algorithm for circular normal inclusion sites as the radius r increases. Fig. 7 shows the density and phase plots for the specific cases with $r = 0.9\xi$, 1.25ξ, 1.75ξ, and 2.2ξ, where the applied current $J = 0$; these results are obtained by solving the TDGL equations. In addition, in Fig. 8, we plot the critical current versus the radius r. From the results, we find that when the inclusion radius r is small, e.g. $r = 0.5\xi$, there are 24 vortices present in the stationary states as was the case in Fig. 1 for $L = 20\xi$ without inclusions; however, the lattice is slightly changed. Furthermore, in this case no vortex is pinned by the inclusion sites. The situation starts to change as r increases because more than one vortex is attracted by each inclusion site, thus changing the structure of the vortex lattice. If the radius is further increased, then additional vortices are pinned by a single inclusion. For example, as can be seen from Fig. 7, when $r = 2.2\xi$ there are six vortices located inside or around each inclusion site. Due to the confinement of the inclusion, these vortices are highly overlapped so that giant holes form at inclusion sites. In addition, Fig. 7 suggests that the size of the normal inclusions also has an influence on the number of vortices in the stationary lattices. As shown in Fig. 1, when $J = 0$, there are 24 vortices in the stationary lattice for $L = 20\xi$, whereas the number becomes 20 when the inclusion radius $r = 0.9\xi$, 1.25ξ and 1.75ξ, and it is 28 if $r = 2.2\xi$.

To see the effect on the critical current, we refer to Fig. 8. If the inclusion radius is in the approximate range $0.75\xi \le r \le 1.9\xi$, we obtain a larger critical current J_c than in the case where there are no inclusion sites. If the radius is too small, e.g. $r = 0.5\xi$, the critical current with four inclusions is much smaller than the case when no inclusions are added. This is because the inclusions are approximately the same size as vortices and are too weak to pin vortices; on the other hand, the interactions of the inclusions and vortices change the structure of the lattice, which may affect the boundary pinning. This phenomenon suggests that larger inclusions should be used to get a better pinning effect. However, inclusion sites which are too large can also reduce the critical current; for example, when $r = 2.3\xi$, the critical current becomes $J_c = 1.6967\text{e}{-4}$ which is much smaller than that of no inclusion. In this case, the normal regions are dominant and the superconductivity becomes very weak, which results in a small critical current.

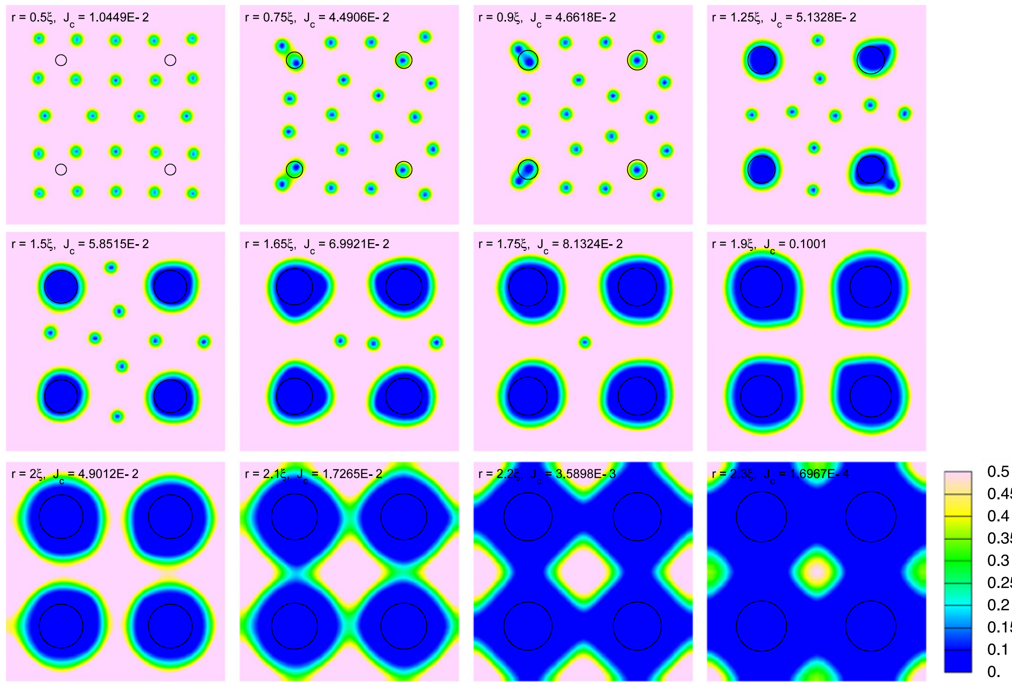

Fig. 6. Vortex pinning and critical current for different inclusion radius r, where the number of normal inclusions is $M = 4$ and the sample size $L = 20\xi$.

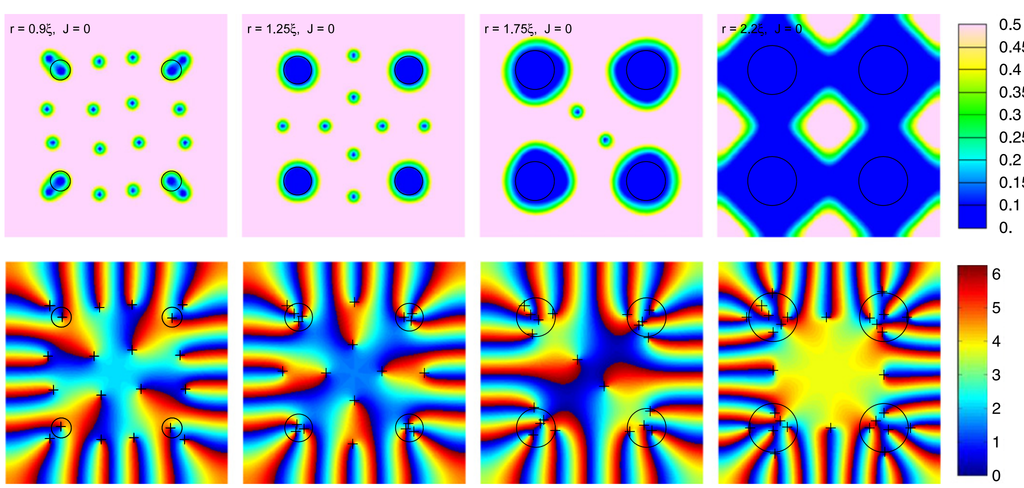

Fig. 7. Density (top) and phase (bottom) plots of stationary vortex lattices when the applied current $J = 0$. From left to right: $r = 0.9\xi$, 1.25ξ, 1.75ξ and 2.2ξ.

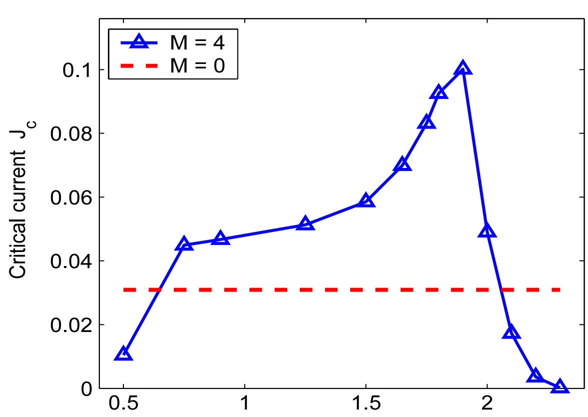

Fig. 8. Critical current J_c versus the normal inclusion radius r, where the locations of the $M = 4$ inclusion sites are fixed and the sample size $L = 20\xi$.

From the above results and those given in Section 4.1.2, we see that usually a higher density of normal inclusions has a stronger pinning of vortices. In this section, the density of normal inclusions is increased by changing their size, whereas in Section 4.1.2, we increased the density by adding more inclusions. Which one is more effective for increasing the critical current J_c? To compare them, Fig. 9 shows the critical current versus the percentage of the sample area occupied by the normal inclusions for the two approaches. This comparison suggests that if we want to keep the impurity pollution small and have as large a critical current as possible, then it is better to have a few larger normal inclusions than many smaller ones, although we also see from Fig. 9 that the critical current is more sensitive to changes in the size of the normal inclusions than to their number.

4.1.4. Effect of shape of inclusion sites

In Sections 4.1.2 and 4.1.3, we examined how the number and the size of circular inclusion sites affect the pinning vortices and the value of the critical current. On the other hand, one might ask if

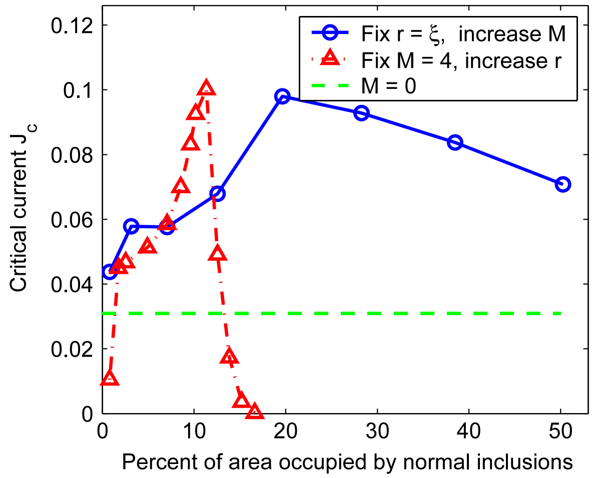

Fig. 9. Critical current J_c for different normal inclusion densities, where the sample size is $L = 20\xi$.

the shape of the normal inclusion sites also influences these factors. In this section, we look at the pinning effect of two additional inclusion shapes, squares and ellipses, and compare the results with those obtained using circular shapes; in addition, we consider different orientations for the elliptical inclusion sites. We enforce the condition that different shaped inclusions have the same area $|D_m| = \pi\xi^2$ as a circular inclusion having radius $r = \xi$. In the case of elliptic shaped inclusions, we choose the length of the major axis to be twice that of the minor axis. As before, the sample size is fixed to be $L = 20\xi$, but now the number of inclusion sites is also fixed as well as are their centres and areas.

Fig. 10 shows vortex pinning and critical currents for $M = 4$ elliptical and square shaped inclusion sites, where different orientations are considered for the elliptically shaped inclusions. Similarly, Figs. 11 and 12 present analogous results for $M = 9$ and 16, respectively. Comparing the results in Figs. 10–12 with those of circular inclusion sites, we find that, in general, the square inclusions have a similar pinning effect as do circular inclusions, and the structure of the resulting lattices is also similar. However, the pinning by the elliptical inclusion sites can be very different for different orientations. For example, for $M = 16$ normal inclusions, the maximum critical current is achieved when the major axes of all the inclusions are parallel to the y-axis. Note that, because the applied current is in the y-direction, all vortices move along the direction parallel to the x-axis so that if the elliptical inclusions are lined up with their major axes perpendicular to that axis, the inclusions act as a wall which impedes the motion of vortices. The above observations suggest that it might be a good approach to pin vortices by embedding thin normal stripes parallel to the direction of the applied current; this, of course, forms a series of Josephson junctions.

4.1.5. *Effect of location of inclusion sites*

In the results presented in the previous sections, the normal inclusions were uniformly distributed in the sample region, and we studied the pinning effect and the critical current by varying the number, size, shape, and orientation of the normal inclusion sites. However, the locations of the inclusion sites also play an important role in the critical current. In [23], this phenomenon was demonstrated on a small sample size of $L = 10\xi$. In Figs. 13–15, we display the stationary vortex lattices and the critical current for $M = 4$, 9, and 16 inclusions, respectively, where the sample size $L = 20\xi$.

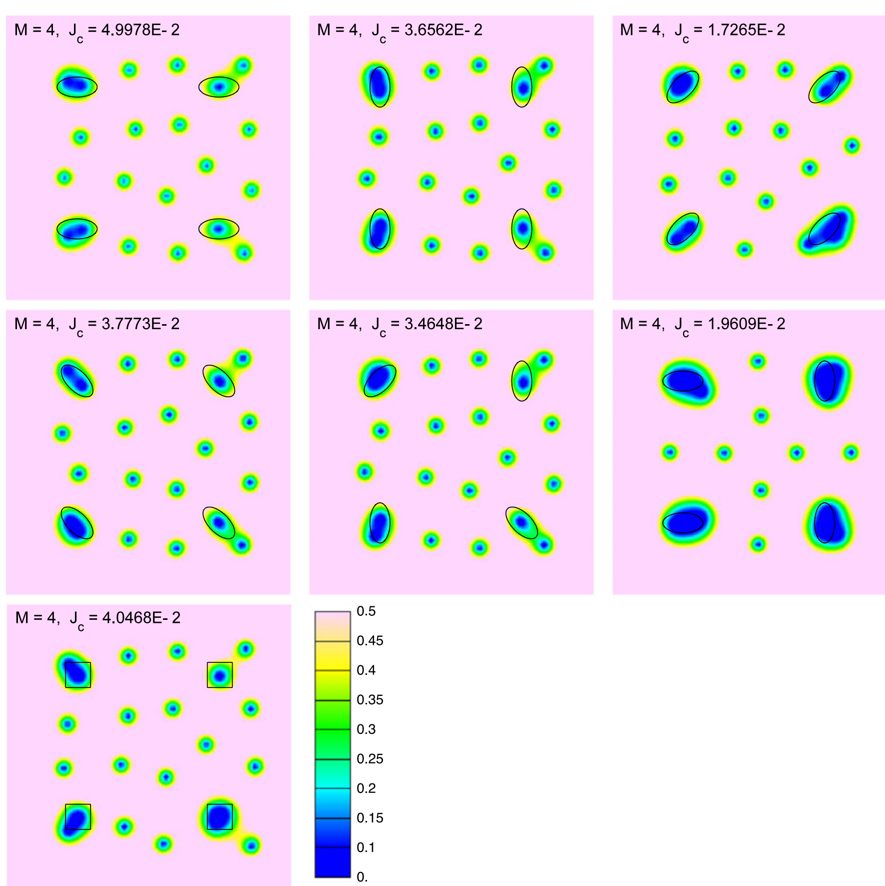

Fig. 10. Vortex pinning and critical current for elliptical and square shaped inclusions, where the number of inclusions is $M = 4$ and all inclusions have the same area $|D_m| = \pi\xi^2$.

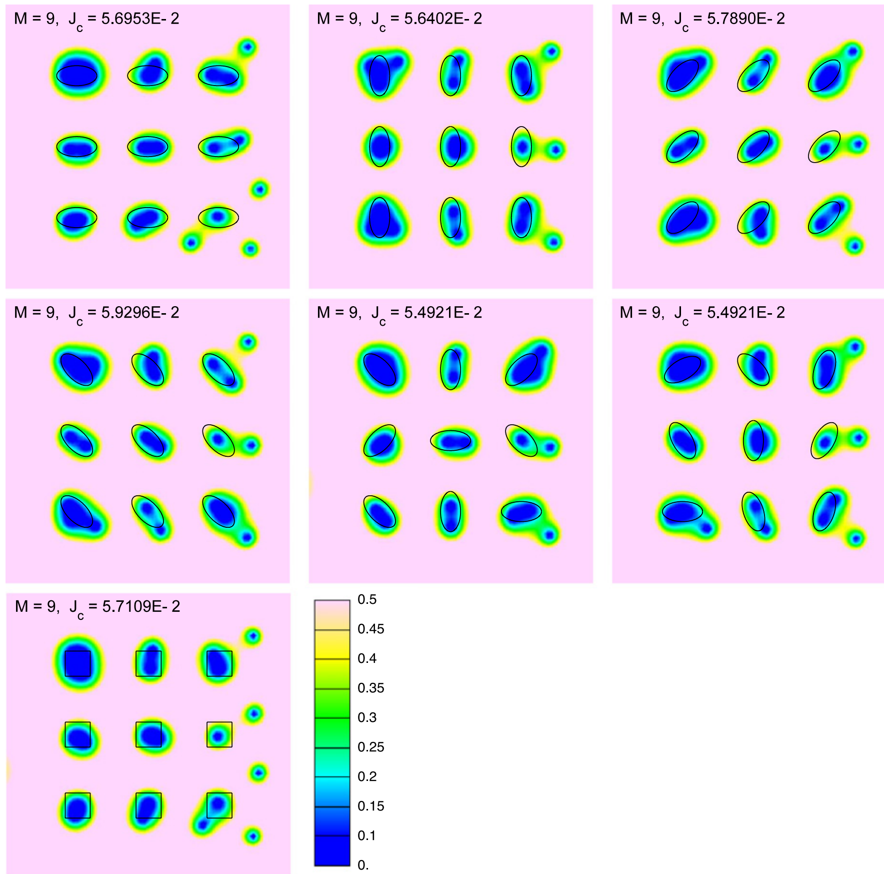

Fig. 11. Vortex pinning and critical current for elliptical and square shaped inclusions, where the number of inclusions is $M = 9$ and all inclusions have the same area $|D_m| = \pi\xi^2$.

These results show that the critical currents for the same number of inclusions may be very different when the locations of inclusion sites are different. For example, in the case of $M = 9$ shown in Fig. 14, the critical current varies from $J_c = 0.0106$ to 0.0659. If the inclusions are inserted around the boundary, the critical current is much smaller than that in a pure superconductor. In contrast, it is significantly increased if all inclusions are distributed on a straight line perpendicular to the x-axis but away from the boundary; see Figs. 14 and 15. Similar to the results in Fig. 12, this intense distribution builds a normal 'wall' which strongly prevents the movement of vortices. These observations again suggest that normal inclusion strips, i.e., Josephson junctions, may have a better pinning effect than the individual inclusions. On the other hand, the phenomena that different inclusion sites yield different values of the critical current suggest that there may be an optimal distribution of normal inclusions, which can provide the best pinning of vortices. This motivates the studies discussed in Section 4.2.

4.2. Studies with multiple optimal control parameters

In Section 4.1, we have seen that the number, size, shape, orientation, and location of impurities influence the critical current. In that section, the optimization process determined the optimal value of the critical current with all parameters that determine the configuration of the inclusions held fixed during that process, i.e., we optimized the cost functional (3.1) only with respect to J. We did this for several values of the parameters that determine the configuration of the inclusions and thus compared the pinning of vortices and critical currents for different configurations.

In this section, we investigate the feasibility of adding additional control or optimization parameters to the optimization problem (3.3). To do this, we use the circular inclusions and require that all inclusion sites have the same radius, i.e., $r_m = r$, for $1 \le m \le M$. A square sample with fixed size of $L = 20\xi$ is considered. The initial guess for the applied current J in the optimization problem (3.3) is chosen as the critical current of the given initial configuration of normal inclusion sites. In the first set of simulations, we fix the locations of the inclusion sites and leave the radius as a control variable, which gives two control parameters, i.e., r and J, in the problem (3.3). In the next set of simulations, the optimization problem is solved by controlling the applied current as well as the location of each inclusion site, whereas their radii are fixed; with M inclusion sites, this gives $2M+1$ optimal parameters. Finally, in Section 4.2.3 we present the results where the radius and locations of inclusion sites, as well as the applied current J, are control parameters, and solve the optimization problem (3.3) with $2M+2$ control parameters, $2M$ for the inclusion locations and one each for the current and the radius of the inclusion sites, recalling that we require all sites to have the same radius.

In the following figures, the dashed circles represent the initial configuration of the normal inclusion sites, whereas the solid ones are the optimal results obtained from the control algorithm.

4.2.1. Optimal size of inclusion sites

In Section 4.1.3, we have seen that for a given configuration of inclusion sites with their locations fixed, varying the radius of the inclusions can result in different critical currents. To better understand the effect the size of the inclusion sites on the critical

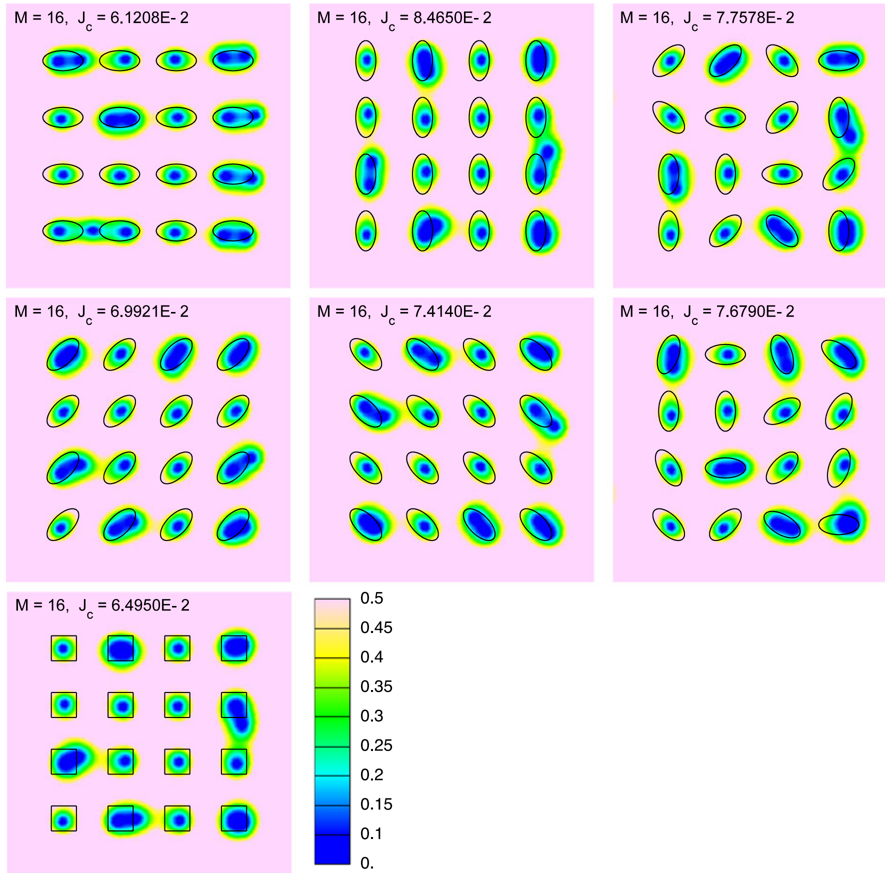

Fig. 12. Vortex pinning and critical current for elliptical and square shaped inclusions, where the number of inclusions is $M = 16$ and all inclusions have the same area $|D_m| = \pi\xi^2$.

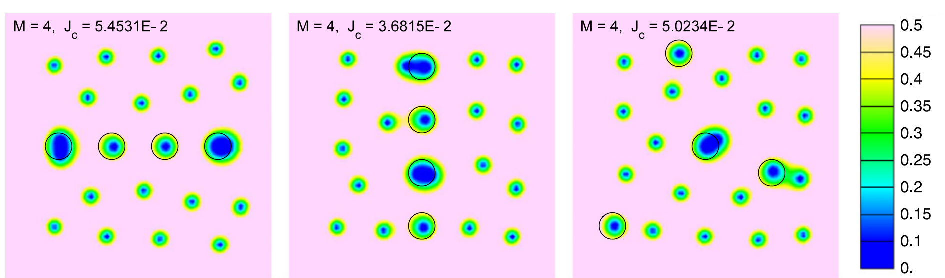

Fig. 13. Vortex pinning and critical current for $M = 4$ normal inclusions having radius $r = \xi$ but having different locations.

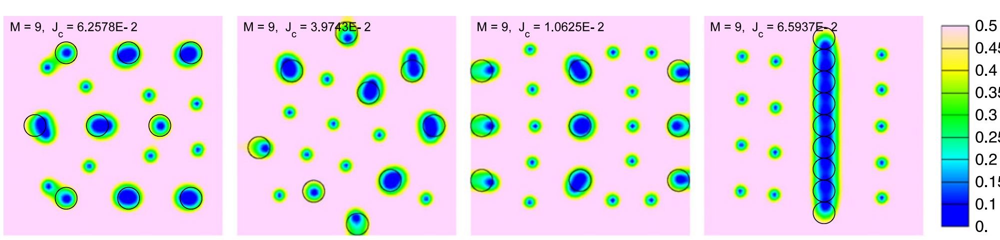

Fig. 14. Vortex pinning and critical current for $M = 9$ normal inclusions having radius $r = \xi$ but having different locations.

current, we consider the radius r of the inclusion as a control parameter and minimize the cost functional (3.1) with respect to two parameters, i.e., r and J. In all cases, we start the control algorithm by choosing the radius $r = \xi$ and the initial applied current to be the critical current corresponding to the initial setting of the inclusion sites.

In Fig. 16, we show the results using $M = 4$ inclusions and compare the initial configurations with those obtained by the control algorithm. Similar results for $M = 9$ and 16 are presented in Figs. 17 and 18, respectively. We find that, in general, the control algorithm yields the results with a larger applied current. However, the increase in the applied current highly depends on the initial locations of the inclusion sites. For example, in Fig. 17, the applied current of the first configuration increases by of approximately 30%, and the optimal radius is much larger than the initial one. For the third case in Fig. 17, the optimal results in both the

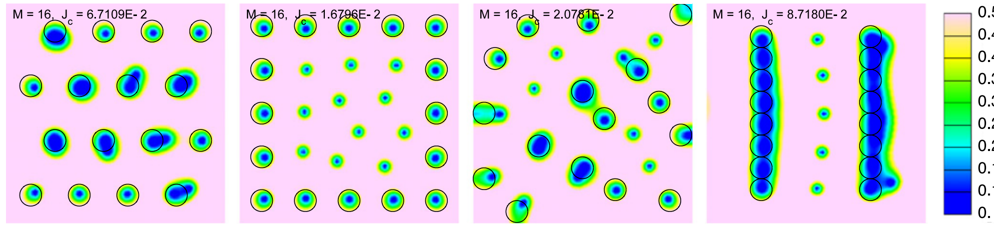

Fig. 15. Vortex pinning and critical current for $M = 16$ normal inclusions having radius $r = \xi$ but having different locations.

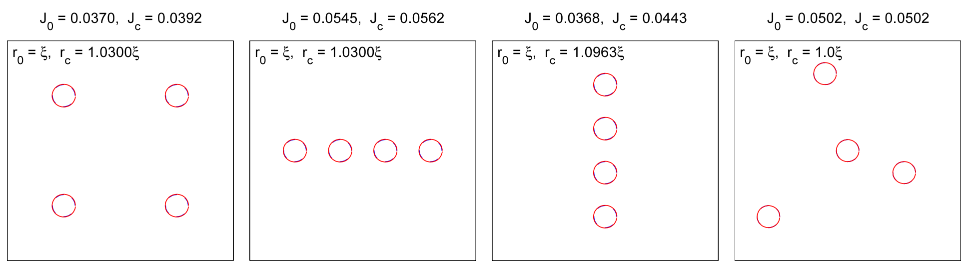

Fig. 16. Initial and optimal configurations of $M = 4$ normal inclusions, where the location of all inclusion sites are fixed, but the radius is a control variable.

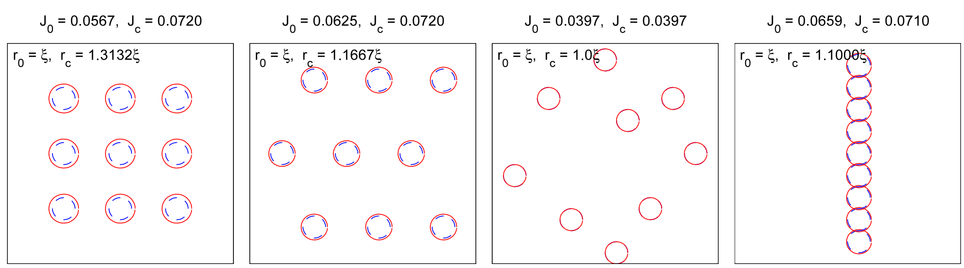

Fig. 17. Initial and optimal configurations of $M = 9$ normal inclusions, where the location of all inclusion sites are fixed, but the radius is a control variable.

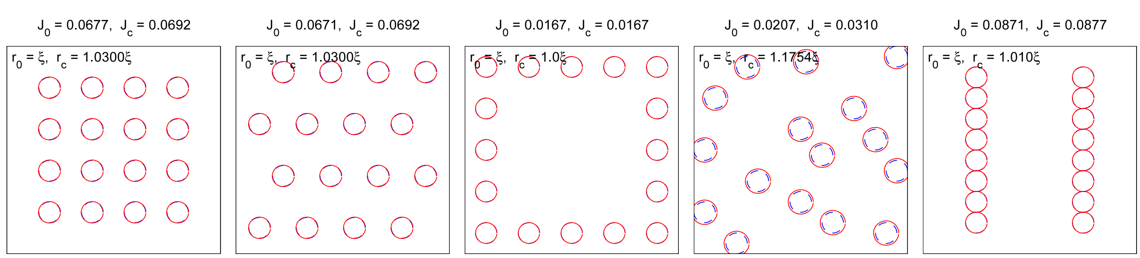

Fig. 18. Initial and optimal configurations of $M = 16$ normal inclusions, where the location of all inclusion sites are fixed, but the radius is a control variable.

applied current and the radius of inclusion sites are quite close to the initial guess. This may be caused by the fact that there are many local minima of the cost functional $\mathcal{F}$ [23], and the cost functional corresponding to the initial configurations is near or at a local minimum. Thus, in this case, the control algorithm leads to the closest minimum point.

4.2.2. Optimal location of inclusion sites

In contrast to the studies in Section 4.2.1, we now fix the radius of the normal inclusions to be $r = \xi$, and then seek the optimal location of those sites so as to maximize the critical current. In this case, the parameter P in (3.2) becomes $P = \{x_m, y_m\}_{m=1}^{M}$ which, along with the current J, means we have $2M + 1$ controls in the optimization problem (3.3); this is, of course, many more than that in Section 4.2.1 where we had only two control parameters. In Figs. 19–21, we illustrate some representative results for the number of inclusion sites $M = 4$, 9, and 16, respectively.

From Figs. 19–21, we see that the critical current is significantly increased by controlling the locations of normal inclusion sites. The control algorithm attempts to move the inclusion sites away from the boundary if their initial locations are close to the sample boundary; see Figs. 20 and 21. These observations agree with those found in Section 4.1.5 that the pinning effect is weak if the inclusion sites are located around the sample boundary.

In addition, if the inclusion sites are initially located along a line perpendicular to the x-axis, then, in the optimal results obtained by the control algorithm, some of the centres are shifted away from this line. To understand this, we notice from Section 4.1.2 that when the number of the normal inclusions is smaller than that of vortices, each inclusion site pins more than one vortex; see Fig. 4. On the other hand, all the vortices carry the same winding number, so they have repulsive interactions on each other. If the inclusion sites align on a line, then they attract all vortices to this line and make the density of vortices around this line high, so that the repulsive interactions are strong. Thus, in this case, to ensure all vortices remain motionless, the pinning sites need to compensate for the forces caused by the application of the current as well as the strong interactions between vortices. The control algorithm adjusts the locations of the inclusion sites away from the line; as a result, it may reduce the interaction force between vortices and allow a large critical current.

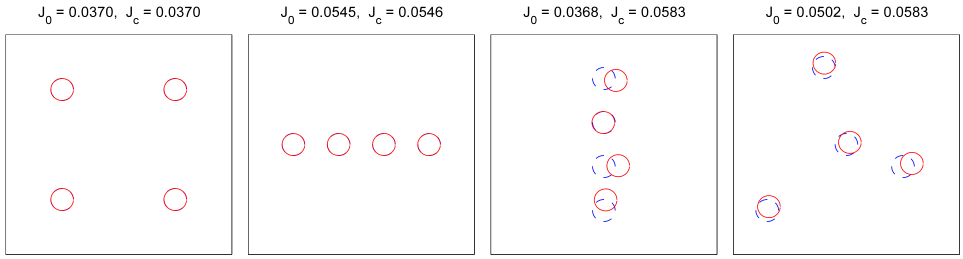

Fig. 19. Initial and optimal configurations of $M = 4$ normal inclusions, where the radius of all inclusion sites is fixed to be $r = \xi$, but the locations are control variables.

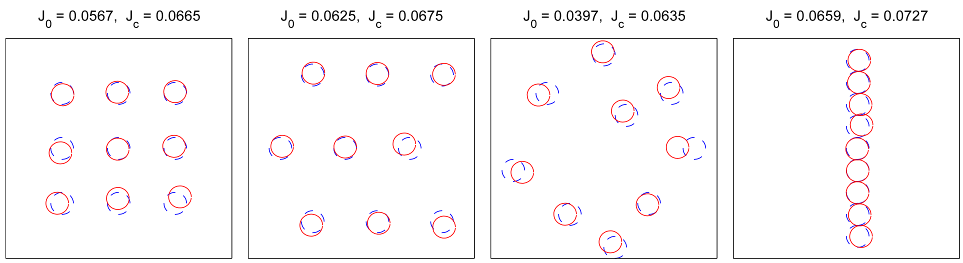

Fig. 20. Initial and optimal configurations of $M = 9$ normal inclusions, where the radius of all inclusion sites is fixed to be $r = \xi$, but the locations are control variables.

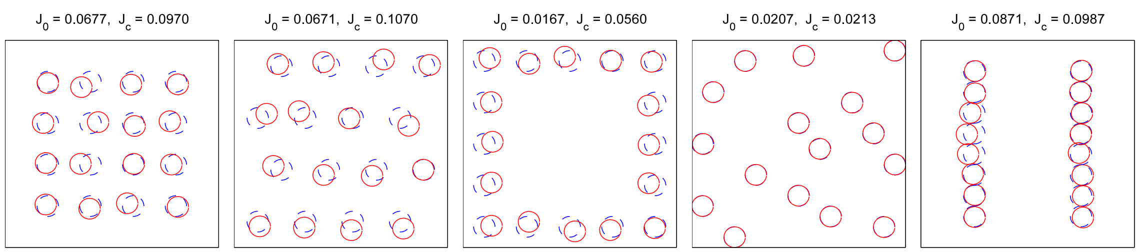

Fig. 21. Initial and optimal configurations of $M = 16$ normal inclusions, where the radius of all inclusion sites is fixed to be $r = \xi$, but the locations are control variables.

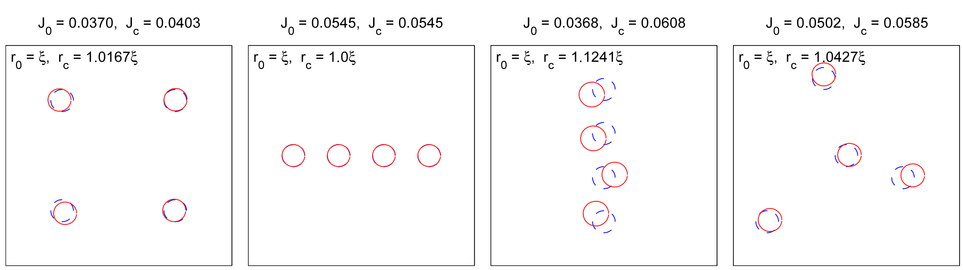

Fig. 22. Initial and optimal configurations of $M = 4$ normal inclusions, where the radius and locations of the inclusion sites are control variables.

4.2.3. Optimal size and location of inclusion sites

In this section, we make a more general study by considering both the radius and the locations of the normal inclusion sites as control parameters. We still require that all inclusion sites have the same radius but allow the radius to change; thus we have $2M + 2$ control parameters in the optimization problem (3.3). Initially, the radius of all M inclusion sites is chosen to be $r = \xi$.

The initial and optimal results are displayed in Figs. 22–24 for the number of inclusion sites $M = 4$, 9, and 16, respectively. The optimal results are quite different from those shown in Sections 4.2.1 and 4.2.2. In addition, numerical computations show that the optimization in this case becomes more difficult than when only the radius or the locations, but not both, serve as control parameters. Note that because the control ranges for the radius r, the location $\mathbf{x}_m$, and the applied current J are all different, we need to use different increments for each kind of control parameter, and thus there are three stepping parameters, i.e. ρ_r, $\rho_{\mathbf{x}}$ and ρ_J. Thus, how to choose a proper set $\{\rho_r, \rho_{\mathbf{x}}, \rho_J\}$ to make an effective control algorithm becomes an important and challenging issue.

5. Summary and discussions

Vortex pinning and the critical current have been studied through an optimal control problem subject to the time-dependent Ginzburg–Landau equations, modified to account for the effect of normal inclusions. We considered a square-shaped superconducting sample and found that its boundaries influence the nucleation of vortices and also have a pinning effect on vortices. Numerical observations suggested that the boundary pinning becomes weaker as the sample size increases; furthermore, the critical current exponentially decays as the sample size is increased.

To study vortex pinning by normal inclusions, we divided our simulations into two parts. In the first part, we chose the applied current as the only control parameter in the optimization problem, and investigated the effect of the number, size, shape, location, and orientation of the inclusion sites on the critical current. We found that, in general, the higher the density of the inclusion sites, the better the pinning effect and the larger the critical current. However, an excessively large number of normal inclusions can

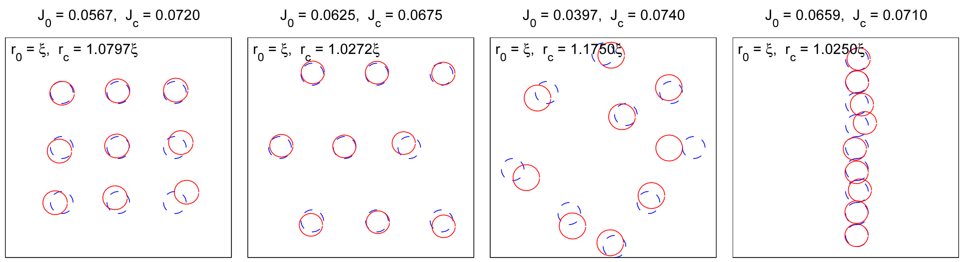

Fig. 23. Initial and optimal configurations of $M = 9$ normal inclusions, where the radius and locations of the inclusion sites are control variables.

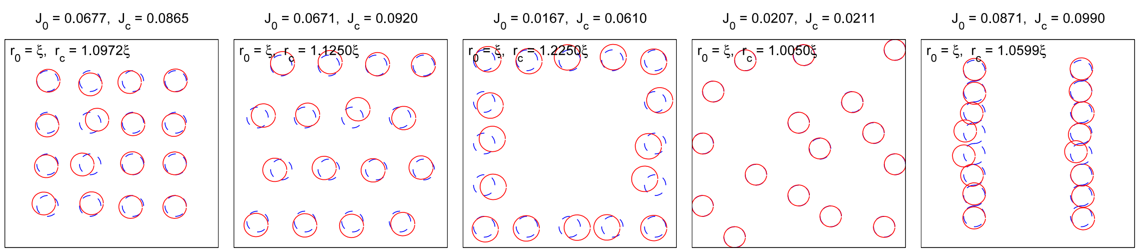

Fig. 24. Initial and optimal configurations of $M = 16$ normal inclusions, where the radius and locations of the inclusion sites are control variable.

reduce the superconductivity of the material and lead to a small critical current. Thus, with all other parameters fixed, there is an optimal density of pinning sites. In addition, simulations suggested that having a few larger normal inclusions is more effective than using many smaller ones to increase the critical current.

In the second part, the radius and the locations of the circular normal inclusion sites were included as the control parameters in addition to the applied current. We studied vortex pinning and the critical current by solving an optimization problem with multiple control parameters. In general, the control algorithm leads to a larger critical current. However, the increase of the critical current highly depends on the initial configurations of the normal inclusion sites. From our numerical simulations, we found that one of the most challenging issues in the current control problem is how to choose the increment for the control parameters at each step, especially when more than one control parameter is involved.

References

[1] S. Dadras, Y. Liu, Y.S. Chai, V. Daadmehr, K.H. Kim, Increase of critical current density with doping carbon nano-tubes in $YBa_2Cu_3O_{7-\delta}$, Physica C 469 (2009) 55–59.
[2] M. Häffner, M. Kemmler, R. Löffler, B. Vega Gómez, M. Fleischer, R. Kleiner, D. Koelle, D.P. Kern, Controlling superconducting properties via vortex pinning by regular arrays of vertical carbon nanotubes, Microelectron. Eng. 86 (2009) 895–897.
[3] A. Mellekh, M. Zouaoui, F. Ben Azzouz, M. Annabi, M. Ben Salem, Nano–Al_2O_3 particle addition effects on $YBa_2Cu_3O_y$ superconducting properties, Solid State Commun. 140 (2006) 318–323.
[4] G.R. Berdiyorov, M.V. Milosević, F.M. Peeters, Vortex configurations and critical parameters in superconducting thin films containing antidot arrays: nonlinear Ginzburg–Landau theory, Phys. Rev. B 74 (2006) 174512.
[5] B. Plourde, D. Harlingen, D. Vodolazov, R. Besseling, M. Hesselberth, P.H. Kes, Influence of edge barriers on vortex dynamics in thin weak-pinning superconducting strips, Phys. Rev. B 64 (2001) 014503.
[6] Q. Du, M. Gunzburger, J. Peterson, Analysis and approximation of the Ginzburg–Landau model of superconductivity, SIAM Rev. 34 (1992) 54–81.
[7] Q. Du, Numerical approximations of the Ginzburg–Landau models of superconductivity, J. Math. Phys. 46 (2005) 095109.
[8] M. Tinkham, Introduction to Superconductivity, Dover, 2004.
[9] S.J. Chapman, Q. Du, M. Gunzburger, A Ginzburg–Landau type model of superconducting/normal junctions including Josephson junctions, Eur. J. Appl. Math. 6 (1995) 97–114.
[10] S.J. Chapman, G. Richardson, Vortex pinning by inhomogeneities in type-II superconductors, Physica D 108 (1997) 397–407.
[11] Q. Du, M. Gunzburger, J. Peterson, Computational simulation of type-II superconductivity including pinning phenomena, Phys. Rev. B 51 (1995) 16194–16203.
[12] N. Nakai, N. Hayashi, M. Machida, Simulation studies for the vortex–depinning dynamics around a columnar defect in superconductor, Physica C 468 (2008) 1270–1273.
[13] J. Deang, Q. Du, M. Gunzburger, J. Peterson, Vortices in superconductors: modelling and computer simulations, Philos. Trans. R. Soc. Lond. A 355 (1997) 1957–1968.
[14] J. Deang, Q. Du, M. Gunzburger, Stochastic dynamics of Ginzburg–Landau vortices in superconductors, Phys. Rev. B 64 (2001) 052506.
[15] J. Deang, Q. Du, M. Gunzburger, Modeling and computation of random thermal fluctuations and material defects in the Ginzburg–Landau model for superconductivity, J. Comput. Phys. 181 (2002) 45–67.
[16] Y. Zhang, W. Bao, Q. Du, Numerical simulation of vortex dynamics in Ginzburg–Landau–Schrödinger equation, Eur. J. Appl. Math. 18 (2007) 607–630.
[17] Y. Zhang, W. Bao, Q. Du, The dynamics and interaction of quantized vortices in Ginzburg–Landau–Schrödinger equation, SIAM J. Appl. Math. 67 (2007) 1775–2740.
[18] W. Bao, R. Zeng, Y. Zhang, Quantized vortex stability and interaction in the nonlinear wave equation, Physica D 237 (2008) 2391–2410.
[19] M. Gunzburger, L. Hou, S. Ravindran, Analysis and approximation of optimal control problems for a simplified Ginzburg–Landau model of superconductivity, Numer. Math. 77 (1997) 243–268.
[20] Z. Chen, K.-H. Hoffmann, Optimal control of dynamical Ginzburg–Landau vortices in superconductivity, Numer. Funct. Anal. Optim. 17 (1996) 241–258.
[21] Z. Chen, K.-H. Hoffmann, Numerical solutions of an optimal control problem governed by a Ginzburg–Landau model in superconductivity, Numer. Funct. Anal. Optimiz. 19 (1998) 737–757.
[22] Y. You, The optimal control of Ginzburg–Landau equations for superconductivity via differential inclusions, Discuss. Math. Differ. Incl. 16 (1996) 5–41.
[23] H. Lin, J. Peterson, M. Gunzburger, Maximizing the critical current in a superconductor through the optimal placement of normal inclusion sites, preprint.
[24] Q. Du, Finite element methods for the time-dependent Ginzburg–Landau model of superconductivity, Comput. Math. Appl. 27 (1994) 119–133.
[25] Q. Du, Global existence and uniqueness of solutions of the time-dependent Ginzburg–Landau model for superconductivity, Appl. Anal. 53 (1994) 1–17.
[26] M. Gunzburger, Perspectives in Flow control and Optimization, SIAM, 2002.
[27] S. Kim, M. Gunzburger, J. Peterson, C.-R. Hu, Computational investigation of the effects of sample geometry on the superconducting-normal phase boundary and vortex-antivortex states in mesoscopic superconductors, Commun. Comput. Phys. 6 (2009) 673–698.
[28] Q. Du, J. Wei, C. Zhao, Vortex solutions of the high-κ high-field Ginzburg–Landau model with an applied current, SIAM J. Math. Anal. 42 (2010) 2368–2401.